

# Strengthening of the concrete face slabs of dams using sprayable strain-hardening fiber-reinforced cementitious composites

Qinghua LI, Xing YIN, Botao HUANG\*, Yifeng ZHANG, Shilang XU

*Institute of Advanced Engineering Structures and Materials, Zhejiang University, Hangzhou 310058, China*

\*Corresponding author. E-mail: botaohuang@zju.edu.cn

© Higher Education Press 2022

**ABSTRACT** In this study, sprayable strain-hardening fiber-reinforced cementitious composites (FRCC) were applied to strengthen the concrete slabs in a concrete-face rockfill dam (CFRD) for the first time. Experimental, numerical, and analytical investigations were carried out to understand the flexural properties of FRCC-layered concrete slabs. It was found that the FRCC layer improved the flexural performance of concrete slabs significantly. The cracking and ultimate loads of a concrete slab with an 80 mm FRCC layer were 132% and 69% higher than those of the unstrengthened concrete slab, respectively. At the maximum crack width of 0.2 mm, the deflection of the 80-mm FRCC strengthened concrete slab was 144% higher than that of the unstrengthened concrete slab. In addition, a FE model and a simplified analytical method were developed for the design and analysis of FRCC-layered concrete slabs. Finally, the test result of FRCC leaching solution indicated that the quality of the water surrounding FRCC satisfied the standard for drinking water. The findings of this study indicate that the sprayable strain-hardening FRCC has a good potential for strengthening hydraulic structures such as CFRDs.

**KEYWORDS** strain-hardening cementitious composites, engineered cementitious composites, sprayable, shotcrete, strengthening, concrete-face rockfill dam, digital image correlation

## 1 Introduction

Concrete-face rockfill dams (CFRDs) have been widely used around the world (over 600 CFRDs existing) owing to their high adaptability, cost efficiency, and reliability. For CFRDs, the concrete slab is used to prevent leakage and act as a structure without concern for uplift pressure. Therefore, the durability and reliability of concrete face slabs are critical for the safety of CFRDs. However, thermal contraction and shrinkage during construction and damage (e.g., earthquakes) during service life may result in cracking of the concrete face slab [1]. Hence, the reduction or prevention of cracks in concrete face slabs is a major concern for CFRDs. To address this challenge, the most frequently used solutions are improvement of the reinforcement ratio in the face slabs, and use of fiber-reinforced concrete instead of ordinary concrete. It was

found that under the same seismic loading, the damage to steel fiber-reinforced concrete face slabs in CFRDs was significantly less than that in ordinary reinforced concrete face slabs [1].

The toughness of ordinary concrete can be improved using fiber reinforcement, but conventional fiber-reinforced concrete (e.g., steel fiber-reinforced concrete) retains tension softening, and its crack resistance is still limited. To realize tensile strain-hardening and high crack resistance of concrete materials, fiber-reinforced cementitious composites (FRCC) with high toughness were developed based on micromechanical principles [2,3]. These materials are named as engineered cementitious composites (ECC) [4–6], strain-hardening cementitious composites (SHCC) [7–9], or ultra-high toughness cementitious composites (UHTCC) [10–12].

For high-toughness FRCC, the compressive strength ranges from 20–80 MPa and the ultimate tensile strain ranges from 1%–7% (100–700 times that of ordinary

concrete) [5,13–15]. Compared with ordinary plain and fiber-reinforced concrete, high-toughness FRCC exhibits superior ductility and crack resistance under monotonic, cyclic (seismic), fatigue, and impact loadings [16–20]. The crack width of high-toughness FRCC is generally below 100  $\mu\text{m}$  under service load and its cracks can be self-healed under environmental conditions (such as those involving wet-dry cycles [21], chloride [22], sulfate [23], high alkaline [24], and acidic environments [25]). These features make high-toughness FRCC an ideal material for applications in hydraulic structures [23,26]. In addition, a sprayable high-toughness FRCC was developed for repair applications [27–31], and it has been successfully applied in the strengthening of hydraulic and transportation infrastructures [29,31]. Typically, a gravity dam in Japan (the Mitaka Dam) was repaired using a 30 mm thick sprayable high-toughness FRCC [26].

Considering the significant potential of high-toughness FRCC in the application of hydraulic structures such as dams, the authors proposed that sprayable high-toughness FRCC could be applied to strengthen reinforced concrete slabs in CFRDs (Fig. 1). With this method, FRCC is employed as an external protective layer of concrete face slabs (on the upstream face, Fig. 1) to fully utilize the excellent crack resistance, ductility, and self-healing performance of FRCC. In addition, the spray process of FRCC makes it very easy to apply the FRCC strengthening layer onto the concrete face slabs. Note that such a method can be used both in the construction and in the repair of CFRDs. As a novel strengthening method, the feasibility of the method requires further proof. First, the flexural performance (particularly the cracking and ultimate loads) of the FRCC-layered concrete face slab should be comprehensively understood; second, the effect of sprayable FRCC on the quality of the surrounding water must be carefully evaluated.

In this research, sprayable high-toughness FRCC was applied to strengthen concrete face slabs in a laboratory. The flexural properties of the FRCC-layered concrete slab was comprehensively investigated using experimental, numerical, and analytical methods. A bending test

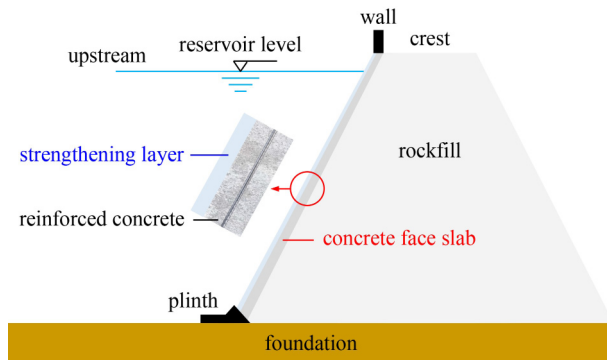


**Fig. 1** Strengthening of concrete-face rockfill dam.

was carried out to investigate the flexural properties of the slabs using different FRCC layer thicknesses. Digital image correlation (DIC) was utilized to analyze the cracks of the slabs. Subsequently, finite element (FE) modeling and a simplified analytical method were used for the analysis of the strengthened slabs. Finally, the leaching solution of the FRCC and ordinary concrete was tested to evaluate the quality of the water surrounding FRCC-layered face slabs. The findings of this study will be very useful for applying sprayable high-toughness FRCC in hydraulic structures such as CFRDs.

## 2 Materials and testing methods

### 2.1 Sprayable high-toughness FRCC

**Raw Materials.** In this study, the mix proportion of the sprayable high-toughness FRCC developed by Huang et al. [31] was used, which has been successfully applied in the strengthening of tunnel lining and bridge slabs. The raw materials included cementitious binders, fine silica sand, water, superplasticizer (SP), hydroxypropyl methylcellulose (HPMC), and polyvinyl alcohol (PVA) fibers. The matrix proportion was cementitious binders: water: silica sand = 1 : 0.3 : 0.2. Note that P·O 52.5 ordinary Portland cement [32] and Class F fly ash were used, and the SP and HPMC were 0.075% and 0.1% (by weight) of the binders, respectively. The sand size was smaller than 0.3 mm. 8-mm PVA fibers were used with a volume fraction of 2.0%. It should be noted that expansion agent was not used in this mix proportion.

**Mixing and Spray Process.** The spray process of the high-toughness FRCC (Fig. 2) was as follows: (I) the cementitious binders and sand were dry-mixed for 1 min; (II) the water, SP, and HPMC were added and mixed for 2 min; (III) the PVA fibers were added and mixed for 2–3 min; (IV) the fresh FRCC was pumped to a spray gun and sprayed. According to the results of the authors'

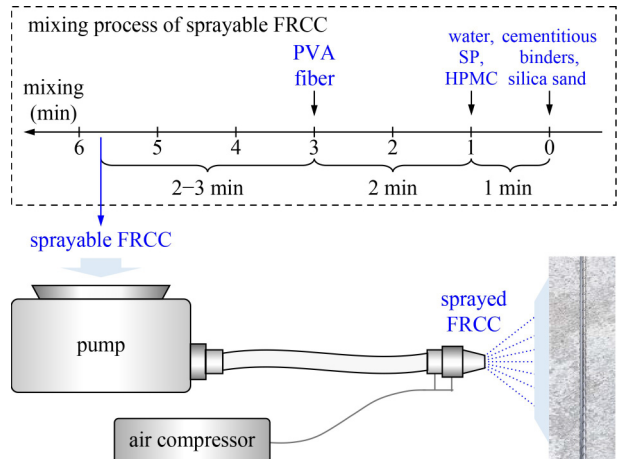


**Fig. 2** Spray process of high-toughness FRCC.

previous study [31], the adhesion of the sprayable FRCC and concrete substrate was adequate, and the rebound rate was < 5% during the spray process.

**Mechanical Performance.** The compressive and tensile performance of the sprayable FRCC was tested after a 28-d normal curing in a curing chamber (temperature: 20°C, relative humidity: 95% [33,34]). The dimensions of the compressive specimen were 100 mm × 100 mm × 100 mm. Figure 3(a) shows the dimensions of tensile specimen (300 mm × 50 mm × 15 mm). These specimens were cut from sprayed FRCC panels [31]. The compressive strength of the sprayable FRCC was 33.0 MPa (loading rate: 5 kN/s). The setup for the tensile test is presented in Fig. 3(a). Carbon fiber sheet and aluminum plate were glued on the specimen with epoxy resin. During the test, two linear variable differential transformers (LVDTs) were utilized to monitor the tensile strain under a loading rate of 0.1 mm/min. The test results are shown in Fig. 3(b). The tensile strength and ultimate tensile strain of the sprayable FRCC were 2.9 MPa and 2.0%, respectively.

**Effect of FRCC on Water Quality.** To evaluate the effect of the sprayable FRCC on the surrounding water, the leaching solution of the FRCC was tested according to the Chinese Standard GB/T 5750.8–2006 [35]. In this test, the FRCC sample was immersed in 1000 mL ultrapure water for 96 h (environmental temperature: 23 °C). To analyze volatile organic compounds (VOC), 30 mL leaching solution was tested using gas chromatography–mass spectrometry (GC–MS). For comparison, an ordinary concrete sample was also tested using the same method.

## 2.2 Experimental program

**Specimens Preparations.** Three groups of reinforced

concrete slabs were prepared and tested. The specimen dimensions are shown in Fig. 4. For all the specimens, the dimensions of the reinforced concrete layers were the same (2200 mm × 400 mm × 500 mm) and the steel reinforcements were placed in the middle. Note that these slabs were designed as the face slabs of CFRDs based on the Chinese Standard SL 228–2013 [36]. According to previous studies on FRCC-layered concrete members [37,38], 50 mm thick FRCC layers were used to strengthen the concrete beams. Thus, in this study, two thicknesses of the FRCC layers (50 and 80 mm in Fig. 4) were considered, and one control group (without an FRCC layer) was also prepared. In the following, the 50 and 80 mm FRCC layers are denoted as S50 and S80, respectively, and the control group as RC. Two specimens were tested for each group. The fabrication process was as follows: (a) steel reinforcements were fixed in timber formwork; (b) commercial concrete was cast into the formwork and cured for 7 d (temperature: 15–20 °C, RH: approximately 75%); (c) the concrete substrate was cleaned using a water jet, and the interface toughness of concrete substrate processed by water jet can be found in Fig. 4; (d) the FRCC layers were sprayed; and (e) the specimens were cured for 28 d. It is noted that due to the space limitation of the curing chamber, the strengthened slabs were cured in the lab and were covered with wet fabrics to control the loss of moisture according to ASTM C31/C31M-19 [39]. The monitored relative humidity near the surface of the specimen was approximately 75%.

**Material Properties.** The sprayable FRCC described in Section 2.1 was used for the FRCC layers of the concrete slabs (Fig. 4). The strength of the commercial concrete was 30.0 MPa. The diameters of longitudinal and transverse bars were 20 mm, and the measured yield

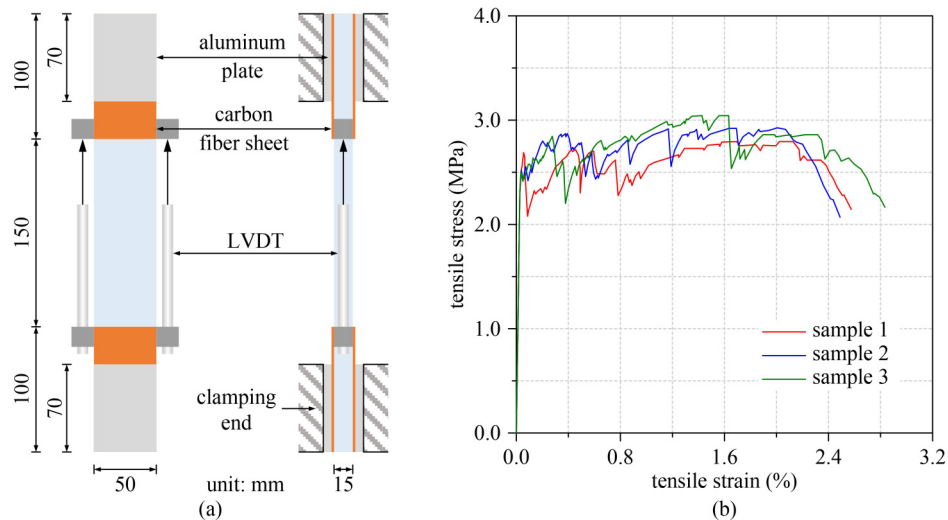


**Fig. 3** Direct tension of sprayable FRCC: (a) setup and (b) tensile behavior. The tensile strength and ultimate tensile strain of sprayable FRCC are 2.9 MPa and 2.0%, respectively.

stress was 510 MPa.

**Test Setup.** The bending test (Fig. 4) was conducted using a 1000-kN INSTRON<sup>TM</sup> system. The slabs were tested under a displacement control of 0.5 mm/min. During the test, a pair of LVDTs was used to measure the deflection at the mid span. It is noted that the RC slab on the upstream of CFRD is subjected to hydrostatic pressure as well as non-uniform gravity loads (i.e., combined flexure and normal force). As the cracking of the RC slab is mainly related to flexural load, this study focused on the strengthening and crack-control performance of high-toughness FRCC in concrete slab under flexural load. In addition, owing to the load of impounding, most of the slab area of CFRD remained in compression, but tensile stresses also developed at the perimeter areas [40]. More importantly, earthquake-induced plastic deformations of dams may result in a significant tensile deformation on the upstream side of a concrete face slab [1]. As the tensile crack at the upstream side is one of the major concerns for the durability and reliability of CFRD, the strengthening performance of FRCC in the tension side was investigated. Note that the flexural performance of FRCC on the compression side is also important for this system. Owing to the enlarged slab section, the use of FRCC can enhance the flexural capacity of the slabs when FRCC is in compression. In future study, to further demonstrate the feasibility of this strengthening method, the case of FRCC in compression needs to be carefully investigated, and the strengthened RC face slab needs to be investigated under the eccentric loading composed of flexure and normal force.

**Digital Image Correlation.** DIC has been utilized in the analysis of the cracking behavior of FRCC materials

[18,41] and FRCC-concrete composite structures [37,38,42]. In this study, DIC was applied to measure the cracks in a zone of length 500 mm (see the central part in Fig. 4), where the speckle pattern was applied. Note that the distance between the two columns of the loading system was 500 mm, which limited the length of the DIC area. During the bending test, light sources were used to highlight this area, and digital photographs were captured every 3 s. In the DIC analysis, the photographs were post-processed using GOM Software 2018.

### 3 Test results and DIC analysis

#### 3.1 Load-deflection behavior and failure mode

Figure 5 shows the load-deflection behavior of S50, S80, and RC, and the average curves are also plotted (S50-avg, S80-avg, and RC-avg). In the lower-right window of Fig. 5, the comparison between the average curves of S50, S80, and RC is shown. It can be observed that the flexural performance of the reinforced concrete slab improved significantly with increasing FRCC thickness. Figure 6 shows the cracking and ultimate loads of RC, S50, and S80. The cracking loads of S50 and S80 were 94% and 132% higher than RC, respectively. The ultimate loads of S50 and S80 were 30% and 69% higher than RC, respectively. The results of Fig. 6 indicated that the FRCC layer strengthened the reinforced concrete slab effectively, and the improvement in the cracking load was significantly higher than that of the ultimate load, owing to the excellent crack resistance of FRCC. In the following sections, the cracking behavior of the specimens will be discussed, and the flexural

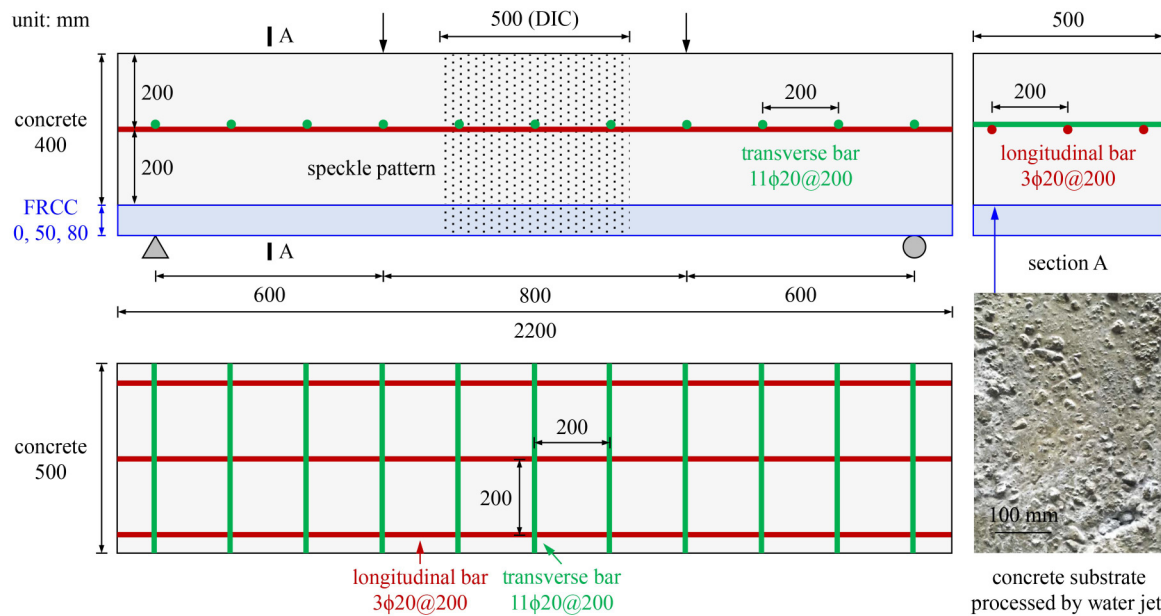


**Fig. 4** Specimen dimensions and test setup.

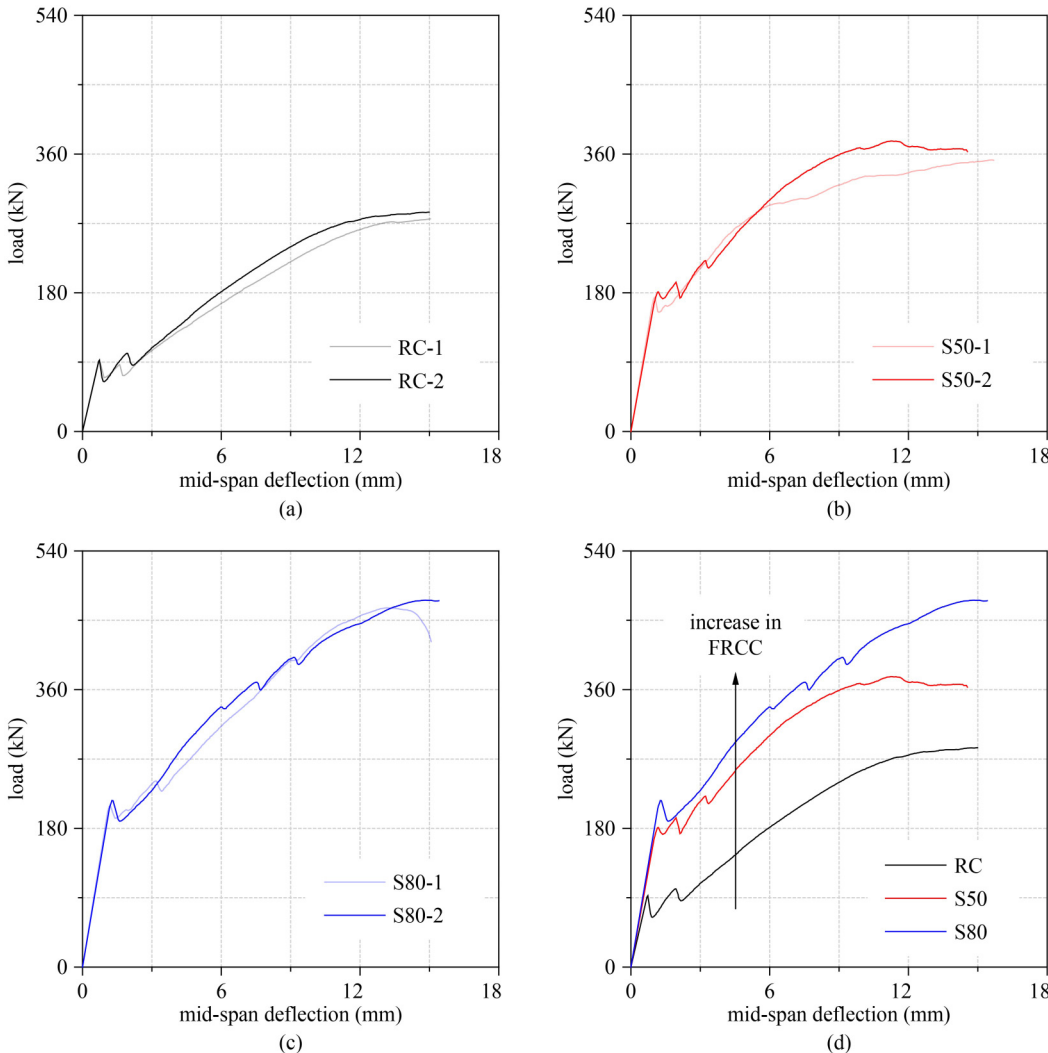


**Fig. 5** Load–deflection curves of (a) RC, (b) S50, and (c) S80. (d) The FRCC layer can enhance the flexural performance of the concrete slabs.

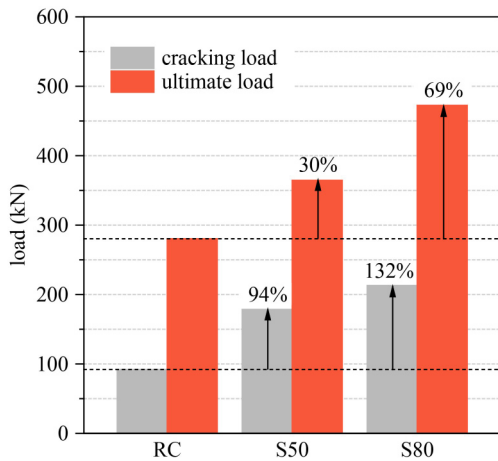


**Fig. 6** Cracking and ultimate loads of RC, S50, and S80. The cracking and ultimate loads of the concrete slabs increase with increase of thickness of the FRCC layer.

performance of the FRCC-layered slabs will be further investigated numerically and analytically.

Figure 7 shows the failure modes of RC, S50, and S80 after the bending test. For all the specimens, flexural failure occurred and no shear cracks were observed. In Fig. 7(a) (the RC specimen), only two cracks were found at the bottom of the specimen. It can be seen that these two cracks propagated from the bottom of the specimen to the position of the longitudinal bar. In addition, many branch-like cracks can be observed near the location of the longitudinal bar. In Figs. 7(b) and 7(c) (the S50 and S80 specimens), the crack patterns of the concrete layer were similar to that of the RC specimen, while the FRCC layers established significant multi-cracking behavior. It should be pointed out that the crack spacing in the concrete layer decreased with increasing thickness of FRCC layer (Fig. 7). Considering the crack control capacity of the FRCC layer, the average crack width of the specimen would decrease with increasing FRCC layer thickness. Thus, at the same mid-span deflection, the crack number would increase and the crack spacing would decrease.

### 3.2 DIC analysis and maximum crack width

To understand the cracking behavior of the specimens at different deflection levels, the DIC results of RC, S50, and S80 are presented in Figs. 8(a)–8(c), respectively. The strain fields at three different deflections are presented for each group. Recall that the steel reinforcements were placed in the middle of the concrete layers, so some cracks can be observed nearby. It is noted that the crack width at the bottom of the RC specimen (Fig. 8(a)) was relatively large, while those of the S50 and S80 specimens were smaller (Figs. 8(b) and 8(c)). In addition, the crack of concrete layer branched into fine cracks of FRCC layer, indicating that the sprayable FRCC layer effectively controlled the concrete cracks. The crack-control performance of the 80 mm FRCC in Fig. 8(c) was superior to that of the 50 mm FRCC in Fig. 8(b). Note that, except for the FRCC/concrete interface near the concrete crack, no interface cracking can be observed, which means that the bond between sprayable FRCC and concrete was reliable during the bending test.

Based the method introduced by Huang et al. [37,38], the maximum crack width of the tested members was monitored using DIC analysis. The maximum crack widths at the bottom of RC, S50, and S80 are plotted in Fig. 9. The crack widths of the slabs strengthened with FRCC layers (S50 and S80) were significantly lower than those of the slabs without the FRCC layer (RC) at the same load level or mid-span deflection. According to the

Chinese Standard SL 775-2018 [43] and GB/T 50476-2019 [44], the limitation of crack width of concrete face slab at the serviceability stage should be no more than 0.2 mm. At the crack widths of 0.2 mm, the loads of RC, S50, and S80 are 87, 191, and 233 kN (Fig. 9(a)), respectively, while the mid-span deflections of RC, S50, and S80 are 1.6, 2.5, and 3.9 mm (Fig. 9(b)), respectively. The FRCC layer improved the load capacity and deflection of concrete face slab at the same crack width. The total crack width is also important for the permeability of strain-hardening FRCC layer [45,46]. At the load level of 280 kN (i.e., the ultimate load of RC group), the total crack widths of RC, S50, and S80 were estimated, and were 11.9, 4.2, and 3.8 mm, respectively. It means that using the FRCC layer also reduced the total crack width of the face slab. As the crack width of a reinforced concrete member is critical for its durability, the use of a sprayable FRCC to strengthen the reinforced concrete slab can enhance the durability and safety of the members and have good potential for applications in CFRDs.

## 4 Finite element modeling

According to the Chinese Standard SL 228–2013 [36], FE analysis is recommended for the design of CFRDs, and the model parameters should be calibrated by experimental results and be appropriately adjusted based on engineering practice. Thus, in order to provide a

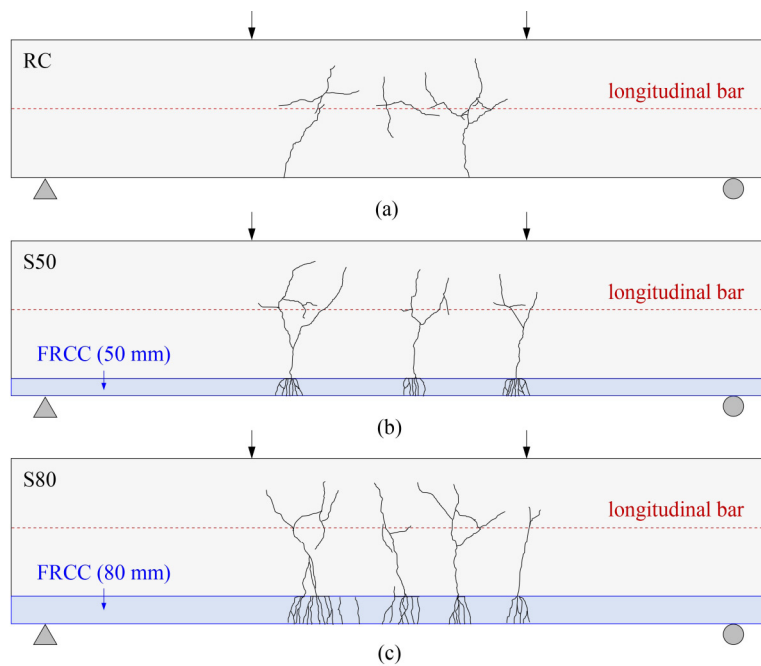


**Fig. 7** Failure modes of (a) RC-1, (b) S50-1, and (c) S80-2. The cracks in the concrete layer are controlled by the FRCC layer effectively.

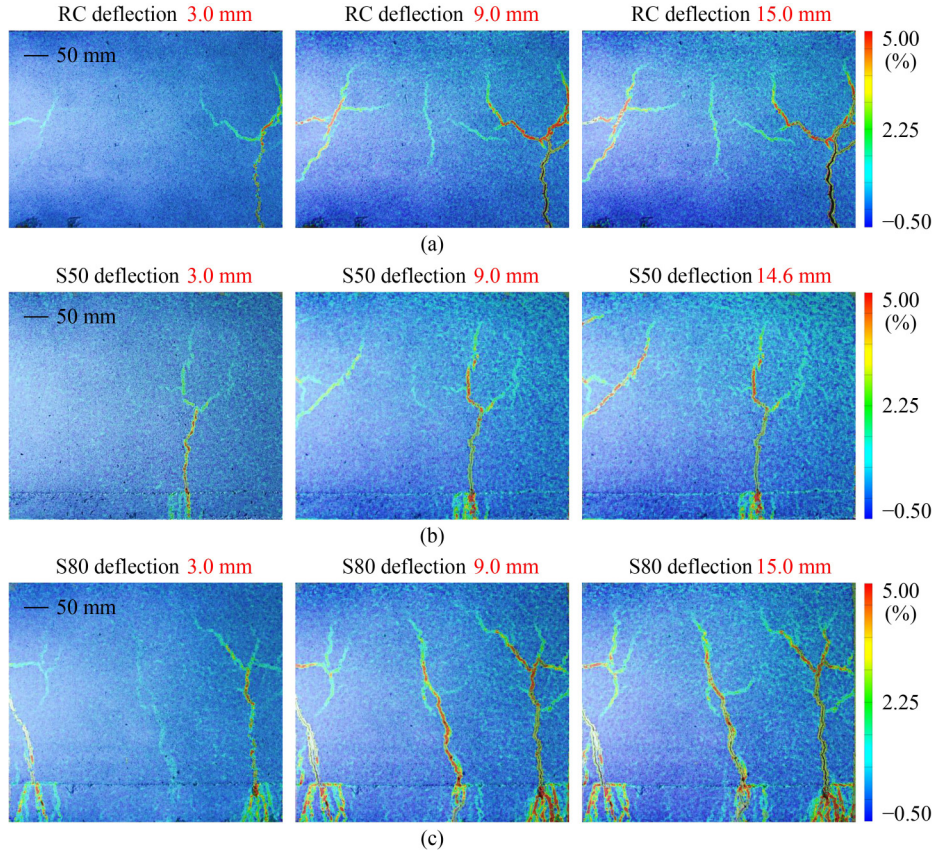


**Fig. 8** Strain fields at different deflections: (a) RC-1, (b) S50-1, and (c) S80-2. Multi-cracking behavior was observed in FRCC and the sprayable FRCC layer effectively controlled the cracking of the concrete layer.

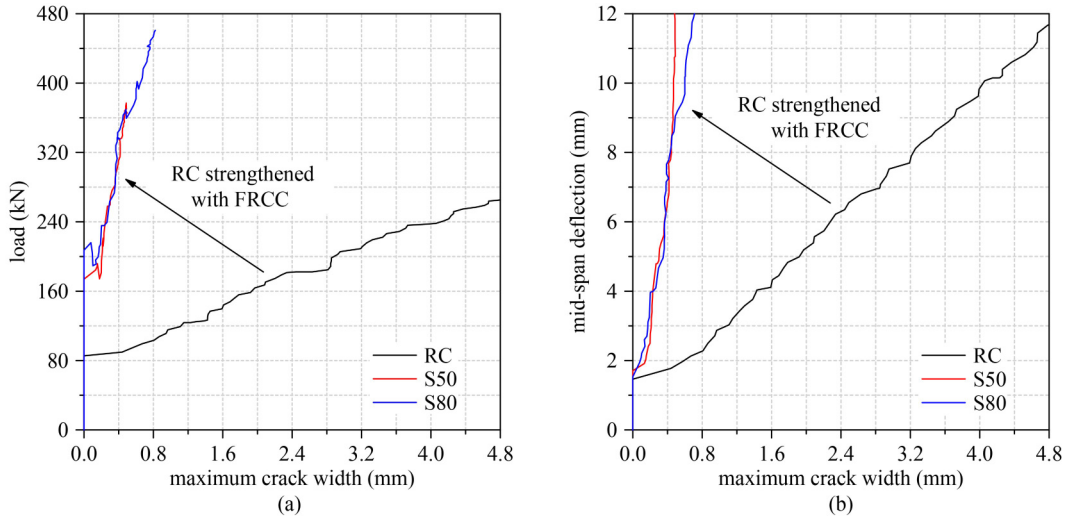


**Fig. 9** (a) Load–maximum crack width relations and (b) mid-span deflection–maximum crack width relations of RC, S50, and S80. The maximum crack widths of the slabs strengthened with FRCC layers (S50 and S80) were significantly lower than that of the slab without an FRCC layer (RC) at the same load or mid-span deflection.

reference for the design of FRCC-strengthened face slabs, a 3D FE model was developed based on ABAQUS [47] to simulate the flexural performance of FRCC-layered concrete slabs. Details and results of the model are presented in the following.

#### 4.1 Constitutive models

The CDP model was utilized for FRCC and ordinary concrete, and the constitutive models are presented in Fig. 10. For a FRCC in compression, the model proposed in Ref. [14] was used (Fig. 10(a)), which can be

expressed as Eq. (1).

$$\sigma_{Fc} = \begin{cases} E_F \varepsilon, & 0 \leq \varepsilon \leq \varepsilon_{Fc1}, \\ E_F \varepsilon (1 - a E_F \varepsilon / \sigma_{Fc2} + b), & \varepsilon_{Fc1} < \varepsilon \leq \varepsilon_{Fc2}, \\ \frac{\sigma_{Fc2} - \sigma_{Fc3}}{\varepsilon_{Fc2} - \varepsilon_{Fc3}} (\varepsilon - \varepsilon_{Fc2}) + \sigma_{Fc2}, & \varepsilon_{Fc2} < \varepsilon \leq \varepsilon_{Fc3}, \\ \frac{\sigma_{Fc3} - \sigma_{Fc4}}{\varepsilon_{Fc3} - \varepsilon_{Fc4}} (\varepsilon - \varepsilon_{Fc3}) + \sigma_{Fc3}, & \varepsilon_{Fc3} < \varepsilon \leq \varepsilon_{Fc4}, \\ \varepsilon_{Fc4} & \end{cases} \quad (1)$$

where  $E_F$  is the FRCC modulus (18 GPa), and  $a$  and  $b$  are 0.308 and 0.124, respectively. The other parameters are listed in Table 1. For a FRCC under tension, a tri-linear model was used (Fig. 10(b)), and the model parameters are listed in Table 1. As the tensile stress vs. cracking opening curve of FRCC has a very long tail [48,49],  $\varepsilon_{Ft3}$  in Fig. 10(b) is assumed to be 4.0% in the FE simulation. In addition, it is found that this value has limited effect on the FE result of the FRCC-layered RC slab. The Poisson's ratio of the sprayable FRCC was 0.17, which was obtained from the experiment performed as part of this study. In addition, the previous study on strain-hardening FRCC also suggested that the Poisson's ratio can be taken as 0.17 [14].

For ordinary concrete, the compressive model presented in Fig. 10(c) was used [50], which can be expressed as Eq. (2).

$$\sigma_{Cc} = \sigma_{Cc1} \left[ 2 \frac{\varepsilon_{Cc}}{\varepsilon_{Cc1}} - \left( \frac{\varepsilon_{Cc}}{\varepsilon_{Cc1}} \right)^2 \right]. \quad (2)$$

The parameters are listed in Table 1. The tensile model in Fig. 10(d) was used to simulate the post-cracking tensile behavior of concrete, and Table 1 also lists the parameters, which were determined according to Refs.

[50,51]. The cracking strain of the concrete was set to 0.00012. For simplicity, the stress-strain relation of concrete was assumed to be linear before tensile cracking. The modulus of elasticity and Poisson's ratio of concrete were 30 GPa and 0.20, respectively.

For both FRCC and concrete, the material dilation angle, shape factor for yield surface, eccentricity parameter, and ratio of the initial equibiaxial compressive yield stress to the initial uniaxial compressive yield stress, were set as 30°, 0.667, 0.1, and 1.16, respectively [52].

The steel reinforcements were modeled using a perfect elastic-plastic model. The modulus of elasticity, yield strength, and yield strain were 200 GPa, 510 MPa, and 0.255% (510 MPa/200 GPa), respectively, and the Poisson's ratio was 0.30.

The bond behavior between steel reinforcements and concrete was modeled by spring elements (SPRING2). In the direction normal to steel reinforcements, two linear spring elements were utilized to prevent the relative displacement between steel bar and concrete, and in the direction parallel to steel reinforcements, the properties of the nonlinear spring elements were defined using the CEB-FIP bond-slip model (Eq. (3) and Fig. 11(a)) [51].

$$\tau_b = \begin{cases} \tau_{bmax} (s/s_1)^\alpha, & 0 \leq s \leq s_1, \\ \tau_{bmax}, & s_1 < s \leq s_2, \\ \tau_{bmax} - (\tau_{bmax} - \tau_{bf})(s - s_2)/(s_3 - s_2), & s_2 < s \leq s_3, \\ \tau_{bf}, & s_3 < s, \end{cases} \quad (3)$$

where  $\tau_{bmax}$  is the bond strength, and the values of the model parameters are listed in Table 2.

The cohesive elements (COH3D8) with traction-separation description (Fig. 11(b)) were created to

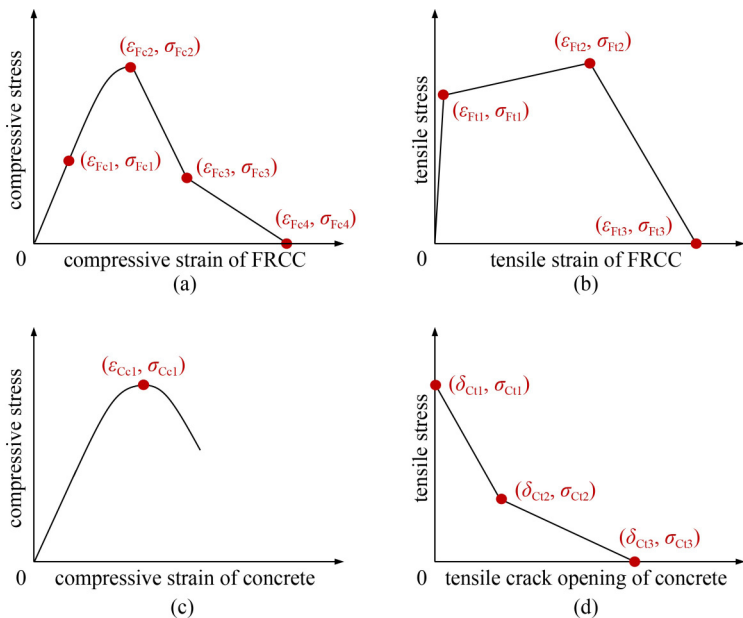


**Fig. 10** Constitutive models of sprayable FRCC (a) in compression and (b) in tension; and concrete (c) in compression and (d) in tension.

simulate the cohesive behavior of the FRCC/concrete interface. In Fig. 11(b), a bi-linear traction-separation description assumes linear elastic behavior, followed by damage initiation. The interface behavior before damage initiation can be expressed using Eq. (4).

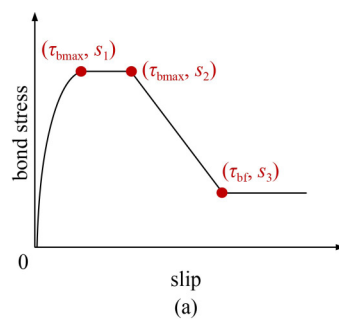
$$\mathbf{T} = \begin{bmatrix} t_n \\ t_s \\ t_t \end{bmatrix} = \begin{bmatrix} K_{nn} & 0 & 0 \\ 0 & K_{ss} & 0 \\ 0 & 0 & K_{tt} \end{bmatrix} \begin{bmatrix} \delta_n \\ \delta_s \\ \delta_t \end{bmatrix} = \mathbf{K}\boldsymbol{\delta}, \quad (4)$$

**Table 1** Parameters in constitutive models of sprayable FRCC and concrete

material	compression	value	tension	value
sprayable FRCC	$\varepsilon_{Fc1}$	0.073%	$\varepsilon_{Ft1}$	0.013%
	$\sigma_{Fc1}$	13.2 MPa	$\sigma_{Ft1}$	2.4 MPa
	$\varepsilon_{Fc2}$	0.282%	$\varepsilon_{Ft2}$	2.000%
	$\sigma_{Fc2}$	33.0 MPa	$\sigma_{Ft2}$	2.9 MPa
	$\varepsilon_{Fc3}$	0.698%	$\varepsilon_{Ft3}$	4.000%
	$\sigma_{Fc3}$	16.5 MPa	$\sigma_{Ft3}$	0
	$\varepsilon_{Fc4}$	4.186%	—	—
	$\sigma_{Fc4}$	0	—	—
concrete	$\varepsilon_{Cc1}$	0.20%	$\delta_{Ct1}$	0
	$\sigma_{Cc1}$	30.0 MPa	$\sigma_{Ct1}$	1.80 MPa
	—	—	$\delta_{Ct2}$	0.05 mm
	—	—	$\sigma_{Ct2}$	0.36 MPa
	—	—	$\delta_{Ct3}$	0.25 mm
	—	—	$\sigma_{Ct3}$	0

**Table 2** Parameters of bond-slip model

parameter	value
$\tau_{bmax}$ (MPa)	15.4
$\tau_{bf}$ (MPa)	6.2
$s_1$ (mm)	1.0
$s_2$ (mm)	2.0
$s_3$ (mm)	8.3
$\alpha$	0.4



(a)

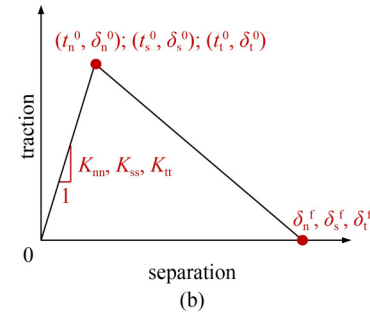
where  $t_n$ ,  $t_s$ , and  $t_t$  are the traction ( $\mathbf{T}$ ) components in normal, shear and tangent directions, respectively;  $K_{nn}$ ,  $K_{ss}$ , and  $K_{tt}$  are their elastic stiffnesses ( $\mathbf{K}$ ); and  $\delta_n$ ,  $\delta_s$ , and  $\delta_t$  are the corresponding interface deformations ( $\boldsymbol{\delta}$ ). In Fig. 11(b),  $\delta_n^f$ ,  $\delta_s^f$ , and  $\delta_t^f$  were set to 10 mm [53]. The maximum normal traction  $t_n^0$  was set to 2.50 MPa, and the maximum tangent tractions  $t_s^0$  and  $t_t^0$  were set to 5.03 MPa, according to the previous study on interface bond between sprayable strain-hardening FRCC and concrete [54]. The tangent slips at maximum tractions  $\delta_s^0$  and  $\delta_t^0$  were set to 0.03 mm, according to the results of FRCC/concrete interface shear test [55]. Finally,  $K_{ss}$  and  $K_{tt}$  were calculated as  $t_s^0/\delta_s^0$  and  $t_t^0/\delta_t^0$ , respectively. According to the suggestion in Ref. [53], the stiffness of the normal traction  $K_{nn}$  was determined as  $K_{nn} = 100K_{ss} = 100K_{tt}$ .

#### 4.2 FE model

Figure 12 shows the 3D FE model of the FRCC-layered concrete slab. The C3D8R (eight node linear brick with reduced integration) elements were used to model the concrete, FRCC, and loading pads (assumed linear elastic) [56], and a two-node linear 3-D truss (T3D2) was used to model the steel reinforcements. The  $x$ -,  $y$ -, and  $z$ -directional mesh lengths were 20, 20, and 25 mm, according to the suggestions in Refs. [50,57]. It is noted that considering the size of coarse aggregate in concrete [50,58], the finer mesh sizes may not suitable for the FE simulation in this study. A tie constraint was employed to make the translational and rotational motions equal for the surfaces of the FRCC and loading pads. The load was applied at the upper loading pads using displacement control.

#### 4.3 Results

The results of FE analysis for RC, S50, and S80 are presented in Figs. 13(a)–13(c), respectively. The simulated results (in red) are very similar to the test results. Both the simulated and tested curves can be divided into two stages. In the first stage, the loads



(b)

**Fig. 11** Interface behavior in FE simulation: (a) bond-slip model of steel reinforcement and concrete; (b) traction-separation constitutive law of the FRCC/concrete interface.

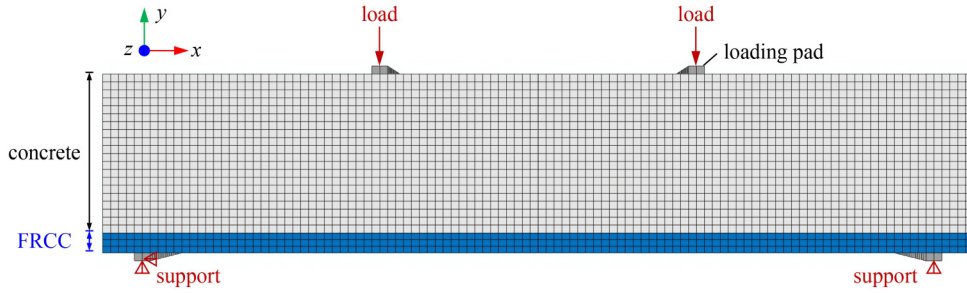


**Fig. 12** 3D FE model of the reinforced concrete slab strengthened with an FRCC layer.

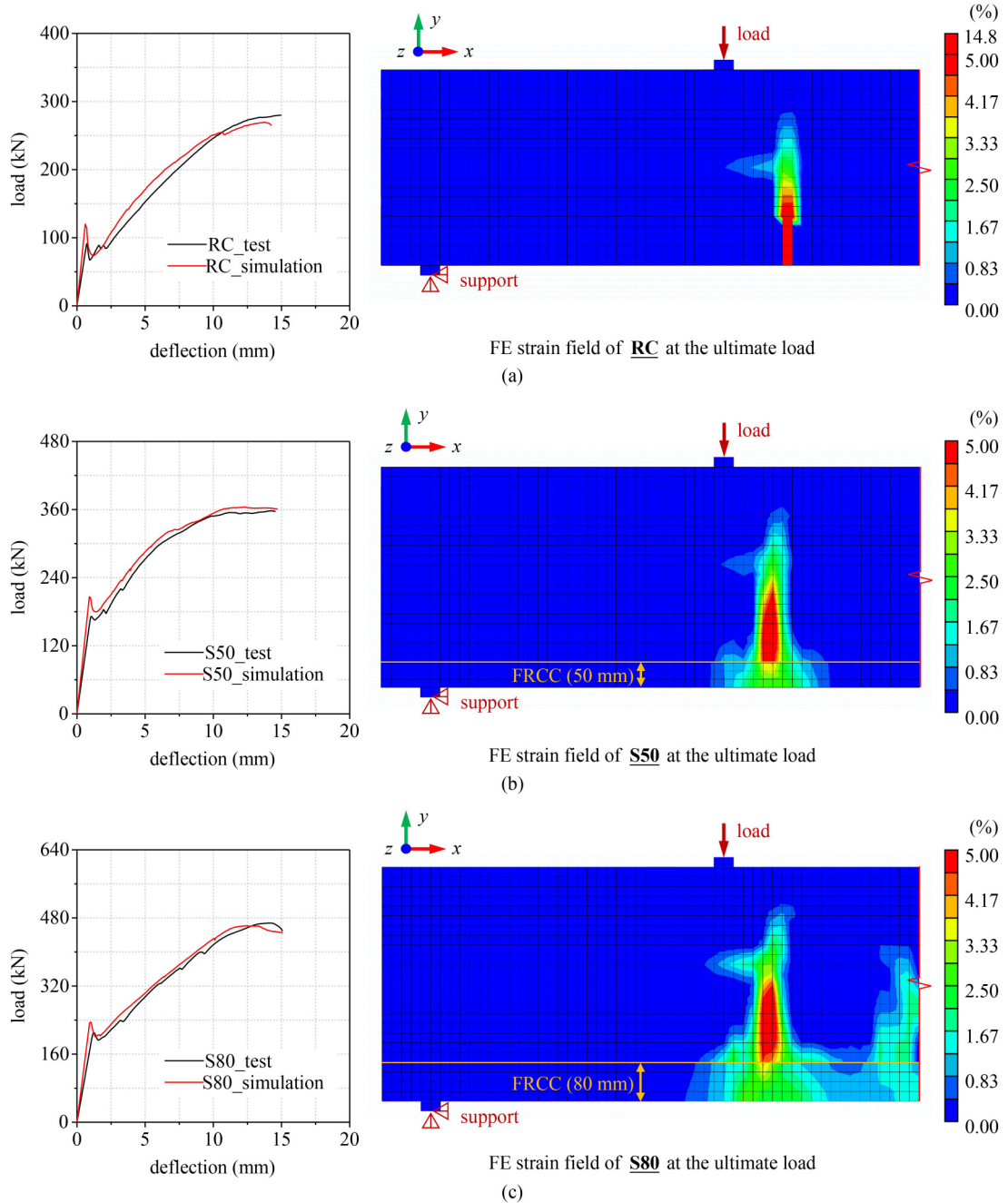


**Fig. 13** Simulation results of (a) RC, (b) S50, and (c) S80. The simulated load–deflection behaviors indicate good agreement with the test ones and the FE strain fields are similar to the DIC results in Fig. 8.

increased almost linearly until the cracking of the concrete layer. In the second stage, the slopes of the curves were smaller than those of the first stage owing to the cracking of concrete and FRCC layers. Overall, the FE model sufficiently captured the full-range load–deflection behaviors of the FRCC-layered reinforced concrete slabs. Moreover, Fig. 13 shows the principal strain fields of the FE analysis. It is noted that the same strain range (i.e., 0%–5%) was set for the principal strain fields of RC, S50, and S80. The maximum strain at the bottom of the concrete layer decreased as the FRCC thickness increased. This indicated that the FRCC layer can aid in controlling the cracks of concrete. In addition, the simulated strain fields were similar to the DIC results in Fig. 8. The FE results (load–deflection curves and principal strain fields) indicated that the developed model could be utilized to predict the flexural properties of FRCC-layered reinforced concrete slabs. The calibrated parameters for FRCC may be useful for simulating the response of the FRCC-RC face slabs. In addition, the FE analysis with the proposed parameters could be utilized to further optimize the design of the strengthened slabs and to simulate the mechanical performance of the slabs under other loading conditions.

It is noted that in this FE modeling, the trilinear tensile stress-strain model of the sprayable FRCC could not reflect the multiple cracking of FRCC layer. Due to the stochastic nature of high-toughness FRCC matrix and the complex micromechanical process of high-toughness FRCC under tension, almost no existing method can be found for the simulation of multiple cracking behavior of high-toughness FRCC in concrete structural members. In future study, it will be important to explore a method for

the accurate simulation of the multiple cracking behavior of high-toughness FRCC in concrete members. Additionally, the maximum crack width is critical for this strengthening system. Accordingly, in future study, one simplified method to estimate the maximum crack width from FE analyses may be as follows: 1) determination of the evolution law of the maximum crack width of sprayable FRCC at different strain levels from direct tensile test; 2) measurement of the simulated tensile strain of FRCC along the bottom of the strengthened slab; and 3) synthesis of the simulated tensile strain measurement and the crack evolution law to obtain the maximum crack width of the FRCC layer in FE analyses. In following study, more efforts are also suggested to realize the accurate simulation of the maximum crack width of FRCC in strengthened members.

## 5 Simplified analytical analysis

In this section, a simplified analytical method is introduced to calculate the cracking and ultimate loads of a reinforced concrete slab with a sprayable FRCC layer. The feasibility of this method is proved by comparing the test and estimated loads. In addition, the effect of the sprayable FRCC layer on the flexural behavior of strengthened slab is discussed.

The strain and stress distributions of the FRCC-layered reinforced concrete slab are shown in Fig. 14 (Fig. 14(a) before cracking of concrete, Fig. 14(b) after cracking of concrete).  $h$  and  $b$  are the height and width of the section, respectively,  $t$  is the thickness of the sprayable FRCC layer,  $m$  is the height of the longitudinal steel

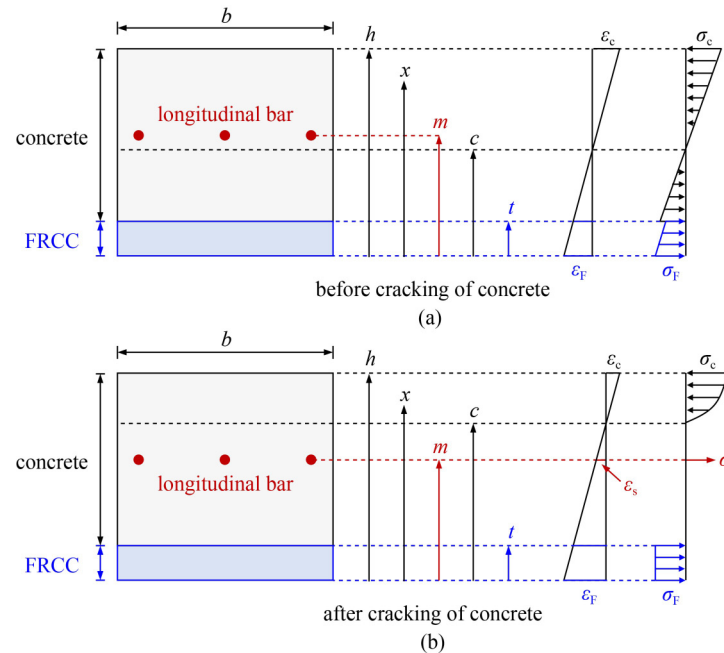


**Fig. 14** Strain and stress distributions of the FRCC-layered reinforced concrete slab (a) before and (b) after the cracking of concrete.

reinforcements,  $c$  is the height of the neutral axis,  $\varepsilon_c$  and  $\sigma_c$  are the strain and stress of the concrete, respectively,  $\varepsilon_F$  and  $\sigma_F$  are the strain and stress of the FRCC, respectively, and  $\varepsilon_s$  and  $\sigma_s$  are the strain and stress of the steel reinforcements, respectively. In Fig. 14(a) (before cracking), the contribution of the steel reinforcements is not considered because they are very close to the neutral axis. Note that the discontinuity point of the stress distribution near the FRCC-concrete interface was caused by the difference in the moduli of FRCC and concrete. In Fig. 14(b) (after cracking), the tensile stress of the concrete below the neutral axis is not considered. For simplicity, the stress of FRCC is assumed to be the same. The feasibility of the above simplifications is proved in the following part.

The cracking and ultimate loads of the FRCC-layered concrete slabs can be estimated based on Fig. 14. The equilibrium equations before cracking of concrete (Fig. 14(a)) can be expressed as follows:

$$\sum N = 0 \Rightarrow \int_c^h b\sigma_c dx = \int_t^c b\sigma_c dx + \int_0^t b\sigma_F dx, \quad (5)$$

$$\begin{aligned} \sum M = 0 \Rightarrow M_{\text{est}} = & \int_c^h b\sigma_c(x-c) dx \\ & + \int_t^c b\sigma_c(x-c) dx + \int_0^t b\sigma_F(x-c) dx, \end{aligned} \quad (6)$$

where  $M_{\text{est}}$  is the estimated bending moment. The values of  $\sigma_c$  and  $\sigma_F$  in Eqs. (5) and (6) were calculated based on the corresponding strain and modulus, and the material parameters in Section 4.1 were also used to calculate the cracking loads of RC, S50, and S80.

The equilibrium equations after cracking of concrete (Fig. 14(b)) can be expressed as follows:

$$\sum N = 0 \Rightarrow \int_c^h b\sigma_c dx = \int_0^t b\sigma_F dx + \sigma_s A_s, \quad (7)$$

$$\begin{aligned} \sum M = 0 \Rightarrow M_{\text{est}} = & \int_c^h b\sigma_c(x-c) dx \\ & + \int_0^t b\sigma_F(x-c) dx + \sigma_s A_s(c-m), \end{aligned} \quad (8)$$

where  $A_s$  is the area of the longitudinal steel reinforcements. To calculate the ultimate loads of RC, S50, and S80, the constitutive model of concrete in Fig. 10(c) was used for  $\sigma_c$ . The steel yield strength (510 MPa) and FRCC tensile strength (2.9 MPa) were used for  $\sigma_s$  and  $\sigma_F$ , and the strain at the bottom of the slab was set to 2.0% (i.e., the tensile strain capacity of high-toughness FRCC).

A comparison of the test and calculated loads is depicted in Fig. 15. Overall, the calculated loads were close to the test loads for both the cracking and ultimate

loads, highlighting the validity of the simplified analytical method. This also indicates that the simplified strain and stress distributions are reasonable. The proposed method can be used in the design and analysis of the flexural performance of the concrete slab with a sprayable FRCC layer.

Recent advances in high-strength strain-hardening FRCC [59,60] facilitate the improvement of their elastic moduli and tensile strengths. In practical applications, a sprayable FRCC with various elastic moduli, tensile strengths, and thicknesses may be used to strengthen reinforced concrete slabs. According to the above analysis, the modulus of elasticity and direct tensile strength of the sprayable FRCC affect the cracking and ultimate loads of the strengthened slab, respectively. Figure 16 shows the effect of these two factors on the increase in cracking and ultimate loads. In Fig. 16,  $E_F$  and  $f_{t-F}$  are the modulus of elasticity (18 GPa) and direct tensile strength (2.9 MPa) of the FRCC used in this study, respectively. The cracking load increases with increasing FRCC modulus. It is noted that the cracking load was calculated based on the ultimate tensile strain of concrete and the assumption of deformation compatibility between FRCC and concrete (see Fig. 14(a)). For the results in Fig. 16(a), the same ultimate tensile strain of concrete was used (i.e., 0.00012). Thus, the larger FRCC modulus means the larger tensile stress of the FRCC layer, which results in the increased cracking load of the FRCC-strengthened specimen under bending load. For a 100 mm thick FRCC with  $1.50E_F$ , the cracking load is improved by approximately 250% (3 times that of the slab without FRCC). For a 100 mm thick FRCC with  $1.50f_{t-F}$ , the ultimate load is improved by approximately 100% (doubling that of the slab without FRCC). In practical applications, the mechanical performance and thickness of FRCC could be adjusted to satisfy diverse requirements.

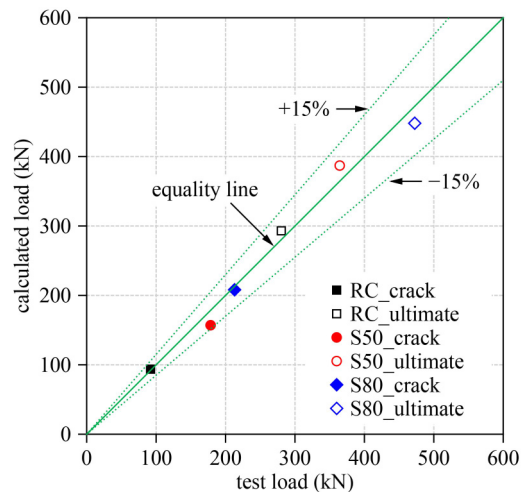


**Fig. 15** Comparison of the test and calculated loads. The calculated loads show good agreement with the test loads.

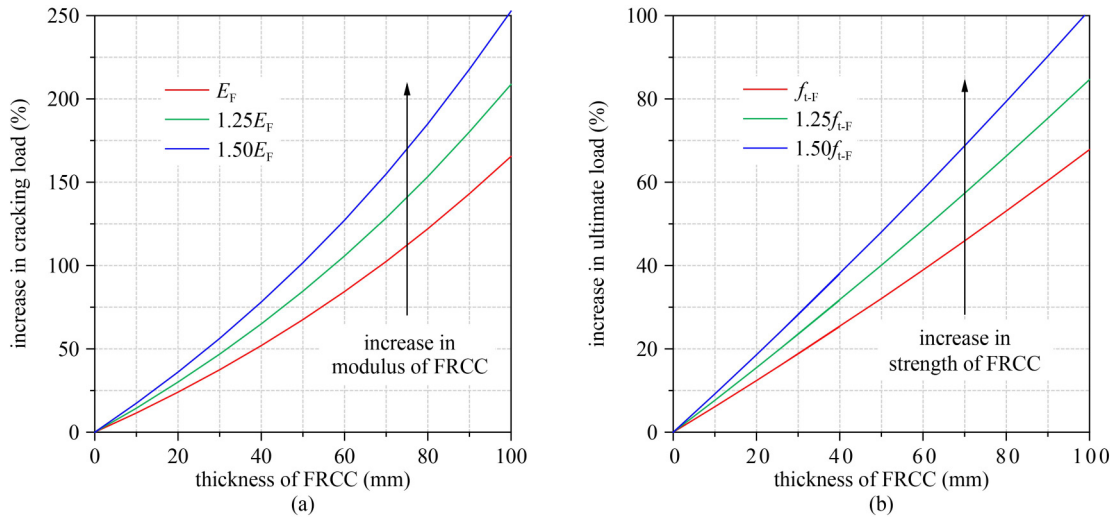


**Fig. 16** (a) Effect of the FRCC modulus ( $E_F$ ) on the cracking load and (b) effect of the tensile strength of FRCC ( $f_{t,F}$ ) on the ultimate load. For the strengthened concrete slabs, the cracking load increases with an increasing FRCC modulus, and the ultimate load increases with an increasing FRCC tensile strength.

## 6 Effect of FRCC on water quality

As an external strengthening layer of CFRD, the effect of a sprayable high-toughness FRCC on the quality of the surrounding water is critical for its practical application. Thus, the VOC in the leaching solution of FRCC and ordinary concrete were tested for comparison (Section 2.1). As listed in Table 3, 23 VOCs were detected in the leaching solution of FRCC and ordinary concrete. The VOC levels of the sprayable FRCC were very similar to those of ordinary concrete. In addition, all the measured VOC levels of FRCC were significantly lower than the limit values in the standard for drinking water [35]. This indicated that the quality of the water surrounding the FRCC was safe for drinking, so the sprayable FRCC can be applied to strengthen concrete face slabs in dams.

## 7 Conclusions and future studies

### 7.1 Conclusions

In this study, sprayable strain-hardening FRCC were used to strengthen concrete slabs in CFRD. The flexural performance of reinforced concrete slabs strengthened using FRCC layers (50 and 80 mm) were investigated experimentally. It was observed that the FRCC layer effectively improved the flexural performance of the slabs. The cracking and ultimate loads of the slabs increased as FRCC thickness increased. The maximum crack width of the slab with the FRCC layer was significantly lower than that of the slab without the FRCC layer at the same load levels. An FE model was developed to simulate the flexural behavior of the FRCC-layered concrete slab, and the numerical results (i.e.,

load-deflection curves and strain fields) had good agreement with the experimental results. In addition, a simplified analytical method was introduced for the design and analysis of the FRCC-layered concrete slabs. It was observed that, for the strengthened slabs, the cracking load increased with increasing FRCC modulus, and the ultimate load increased with increasing FRCC tensile strength. Finally, the test result of the FRCC leaching solution indicated that the quality of the water surrounding FRCC satisfied the standard for drinking water.

### 7.2 Recommendations for future study

According to the findings of this study, the sprayable FRCC can be used to strengthen concrete face slabs in dams. In future study, to further demonstrate the feasibility of this strengthening method, the strengthening performance of the FRCC layer on the compression side of the slab should be investigated. Also, the FRCC-layered RC slab needs to be investigated under the eccentric loading composed of flexure and normal force, because the RC face slab of CFRD is subjected to hydrostatic pressure as well as non-uniform gravity loads. The durability performance of FRCC-layered concrete slabs is suggested to be validated comprehensively, including investigation of frost resistance, impermeability with cracked and uncracked FRCC layers, self-healing performance of the FRCC strengthening layer, and long-term mechanical performance of the strengthened slab. It is noted that for FRCC in hydraulic applications, water submerged curing is more appropriate than moisture curing. Thus, water submerged curing is strongly suggested for future study.

**Table 3** VOC levels in the leaching solution of FRCC and ordinary concrete (mg/L)

No.	VOC	standard for drinking water [35]	sprayable FRCC	ordinary concrete
1	Chloroform	0.0600	0.0040	0.0044
2	Tribromomethane	0.1000	0.0049	0.0048
3	Dibromochloromethane	0.1000	0.0029	0.0029
4	Bromodichloromethane	0.0600	0.0023	0.0023
5	Trihalomethane (total)	1.0000	0.1824	0.1876
6	Trans-1,2-Dichloroethene	0.0500	0.0009	0.0009
7	Cis-1,2-Dichloroethylene	0.0500	0.0013	0.0018
8	1,1-Dichloroethene	0.0300	0.0014	0.0014
9	Vinyl Chloride	0.0050	0.0021	0.0021
10	Trichloroethylene	0.0700	0.0037	0.0037
11	Perchloroethylene	0.0400	0.0048	0.0048
12	Hexachlorobutadiene	0.0006	0.0053	0.0053
13	Dichloromethane	0.0200	0.0110	0.0137
14	Carbon Tetrachloride	0.0020	0.0020	0.0020
15	1,2-Dichloroethane	0.0300	0.0014	0.0014
16	1,1,1-Trichloroethane	2.0000	0.0017	0.0017
17	Toluene	0.7000	0.0006	0.0003
18	Ethylbenzene	0.3000	0.0004	0.0003
19	Chlorobenzene	0.3000	0.00003	0.00002
20	1,2-Dichlorobenzene	1.0000	0.0005	0.0005
21	1,4-Dichlorobenzene	0.3000	0.0004	0.0004
22	Styrene	0.0200	0.0004	0.0004
23	Xylene	0.5000	0.0003	0.0003

**Acknowledgements** This study was financially supported by the National Natural Science Foundation of China (Grant Nos. 51978607 and 51878601). The authors would like to thank Mr. Xiao-Hua Ji and Dr. Fu-Jiang Mu at Zhejiang University for their support in the experiments.

## References

- Qu Y, Zou D, Kong X, Liu J, Zhang Y, Yu X. Seismic damage performance of the steel fiber reinforced face slab in the concrete-faced rockfill dam. *Soil Dynamics and Earthquake Engineering*, 2019, 119: 320–330
- Li V C, Leung C K Y. Steady-state and multiple cracking of short random fiber composites. *Journal of Engineering Mechanics*, 1992, 118(11): 2246–2264
- Leung C K Y. Design criteria for pseudoductile fiber-reinforced composites. *Journal of Engineering Mechanics*, 1996, 122(1): 10–18
- Li V C. Engineered Cementitious Composites (ECC)—Bendable Concrete for Sustainable and Resilient Infrastructure. Berlin: Springer-Verlag GmbH Germany, 2019
- Huang B T, Yu J, Wu J Q, Dai J G, Leung C K Y. Seawater sea-sand Engineered Cementitious Composites (SS-ECC) for marine and coastal applications. *Composites Communications*, 2020, 20: 100353
- Huang B T, Wu J Q, Yu J, Dai J G, Leung C K Y, Li V C. Seawater sea-sand engineered/strain-hardening cementitious composites (ECC/SHECC): Assessment and modeling of crack characteristics. *Cement and Concrete Research*, 2021, 140: 106292
- Lin X, Yu J, Li H, Lam J Y K, Shih K, Sham I M L, Leung C K Y. Recycling polyethylene terephthalate wastes as short fibers in strain-hardening cementitious composites (SHCC). *Journal of Hazardous Materials*, 2018, 357: 40–52
- Huang B T, Li Q H, Xu S L, Zhang L. Static and fatigue performance of reinforced concrete beam strengthened with strain-hardening fiber-reinforced cementitious composite. *Engineering Structures*, 2019, 199: 109576
- Lorenzoni R, Curosu I, Leonard F, Paciornik S, Mechtherine V, Silva F A, Bruno G. Combined mechanical and 3D-microstructural analysis of strain-hardening cement-based composites (SHCC) by *in-situ* X-ray microtomography. *Cement and Concrete Research*, 2020, 136: 106139
- Xu S L, Li Q. Theoretical analysis on bending behavior of functionally graded composite beam crack-controlled by ultrahigh toughness cementitious composites. *Science in China Series E: Technological Sciences*, 2009, 52(2): 363–378
- Huang B T, Li Q H, Xu S L, Zhou B M. Frequency effect on the compressive fatigue behavior of ultrahigh toughness cementitious

- composites: Experimental study and probabilistic analysis. *Journal of Structural Engineering*, 2017, 143(8): 04017073
12. Huang B T, Li Q H, Xu S L, Liu W, Wang H T. Fatigue deformation behavior and fiber failure mechanism of ultra-high toughness cementitious composites in compression. *Materials and Design*, 2018, 157: 457–468
  13. Wang S, Li V C. Engineered cementitious composites with high-volume fly ash. *ACI Materials Journal*, 2007, 104(3): 233–241
  14. Zhou J, Pan J, Leung C K Y. Mechanical behavior of fiber-reinforced engineered cementitious composites in uniaxial compression. *Journal of Materials in Civil Engineering*, 2015, 27(1): 04014111
  15. Huang B T, Li Q H, Xu S L. Fatigue deformation model of plain and fiber-reinforced concrete based on Weibull function. *Journal of Structural Engineering*, 2019, 145(1): 04018234
  16. Yuan F, Pan J, Xu Z, Leung C K Y. A comparison of engineered cementitious composites versus normal concrete in beam-column joints under reversed cyclic loading. *Materials and Structures*, 2013, 46(1): 145–159
  17. Qiu J, Yang E H. Micromechanics-based investigation of fatigue deterioration of engineered cementitious composite (ECC). *Cement and Concrete Research*, 2017, 95: 65–74
  18. Huang B T, Weng K F, Zhu J X, Xiang Y, Dai J G, Li V C. Engineered/strain-hardening cementitious composites (ECC/SHCC) with an ultra-high compressive strength over 210 MPa. *Composites Communications*, 2021, 26: 100775
  19. Curosu I, Mechtkerine V, Forni D, Cadoni E. Performance of various strain-hardening cement-based composites (SHCC) subject to uniaxial impact tensile loading. *Cement and Concrete Research*, 2017, 102: 16–28
  20. Huang B T, Li Q H, Xu S L, Zhou B M. Tensile fatigue behavior of fiber-reinforced cementitious material with high ductility: Experimental study and novel P-S-N model. *Construction and Building Materials*, 2018, 178: 349–359
  21. Yang Y, Lepech M D, Yang E H, Li V C. Autogenous healing of engineered cementitious composites under wet–dry cycles. *Cement and Concrete Research*, 2009, 39(5): 382–390
  22. Li M, Li V C. Cracking and healing of engineered cementitious composites under chloride environment. *ACI Materials Journal*, 2011, 108(3): 333–340
  23. Liu H, Zhang Q, Gu C, Su H, Li V. Self-healing of microcracks in engineered cementitious composites under sulfate and chloride environment. *Construction and Building Materials*, 2017, 153: 948–956
  24. Shahmaran M, Li V C. Durability of mechanically loaded engineered cementitious composites under highly alkaline environments. *Cement and Concrete Composites*, 2008, 30(2): 72–81
  25. Wu H L, Du Y J, Yu J, Yang Y L, Li V C. Hydraulic conductivity and self-healing performance of engineered cementitious composites exposed to acid mine drainage. *Science of the Total Environment*, 2020, 716: 137095
  26. Kunieda M, Rokugo K. Recent progress on HPFRCC in Japan. *Journal of Advanced Concrete Technology*, 2006, 4(1): 19–33
  27. Kim Y Y, Kong H J, Li V C. Design of engineered cementitious composite suitable for wet-mixture shotcreting. *Materials Journal*, 2003, 100(6): 511–518
  28. Kanda T, Saito T, Sakata N, Hiraishi M. Tensile and anti-spalling properties of direct sprayed ECC. *Journal of Advanced Concrete Technology*, 2003, 1(3): 269–282
  29. Rokugo K, Kanda T, Yokota H, Sakata N. Applications and recommendations of high performance fiber reinforced cement composites with multiple fine cracking (HPFRCC) in Japan. *Materials and Structures*, 2009, 42(9): 1197–1208
  30. Zhang Q, Li V C. Development of durable spray-applied fire-resistant Engineered Cementitious Composites (SFR-ECC). *Cement and Concrete Composites*, 2015, 60: 10–16
  31. Huang B T, Li Q H, Xu S L, Zhou B. Strengthening of reinforced concrete structure using sprayable fiber-reinforced cementitious composites with high ductility. *Composite Structures*, 2019, 220: 940–952
  32. China National Standardization Management Committee. Common Portland Cement: GB 175–2007. Beijing: Standards Press of China, 2007 (in Chinese)
  33. Ministry of Housing and Urban-Rural Development of the People's Republic of China. Standard for Test Methods of Concrete Physical and Mechanical Properties: GB/T 50081-2019. Beijing: China Architecture & Building Press, 2019 (in Chinese)
  34. ISO. Testing of concrete—Part 3: Making and curing test specimens: ISO 1920-3: 2019. Geneva: International Organization for Standardization, 2019
  35. Ministry of Health of the People's Republic of China. Standard Examination Methods for Drinking Water—Organic Parameters: GB/T 5750.8–2006. Beijing: Standards Press of China, 2006 (in Chinese)
  36. Ministry of Water Resources of the People's Republic of China. Design Code for Concrete Face Rockfill Dams: SL 228–2013. Beijing: China Water & Power Press, 2013 (in Chinese)
  37. Huang B T, Li Q H, Xu S L, Li C F. Development of reinforced ultra-high toughness cementitious composite permanent formwork: Experimental study and digital image correlation analysis. *Composite Structures*, 2017, 180: 892–903
  38. Huang B T, Dai J G, Weng K F, Zhu J X, Shah S P. Flexural performance of UHPC–concrete–ECC composite member reinforced with perforated steel plates. *Journal of Structural Engineering*, 2021, 147(6): 04021065
  39. ASTM. Standard Practice for Making and Curing Concrete Test Specimens in the Field: ASTM C31/C31M–19. West Conshohocken: ASTM International, 2019
  40. Mahabad N M, Imam R, Javanmardi Y, Jalali H. Three-dimensional analysis of a concrete-face rockfill dam. *Proceedings of the Institution of Civil Engineers-Geotechnical Engineering*, 2014, 167(4): 323–343
  41. Xu L Y, Huang B T, Dai J G. Development of engineered cementitious composites (ECC) using artificial fine aggregates. *Construction & Building Materials*, 2021, 305: 124742
  42. Huang B T, Zhu J X, Weng K F, Li V C, Dai J G. Ultra-high-strength engineered/strain-hardening cementitious composites (ECC/SHCC): Material design and effect of fiber hybridization. *Cement and Concrete Composites*, 2022, 129: 104464
  43. Ministry of Water Resources of the People's Republic of China. Specification for Evaluating Durability of Hydraulic Concrete

- Structures: SL 775-2018. Beijing: China Water & Power Press, 2018 (in Chinese)
44. Ministry of Housing and Urban-Rural Development of the People's Republic of China. Standard for Design of Concrete Structure Durability: GB/T 50476-2019. Beijing: China Architecture & Building Press, 2019 (in Chinese)
  45. Paul S C, van Zijl G P A G. Mechanically induced cracking behaviour in fine and coarse sand strain hardening cement based composites (SHCC) at different load levels. *Journal of Advanced Concrete Technology*, 2013, 11(11): 301–311
  46. Paul S C, van Zijl G P A G. Crack formation and chloride induced corrosion in reinforced strain hardening cement-based composite (R/SUCC). *Journal of Advanced Concrete Technology*, 2014, 12(9): 340–351
  47. Dassault Systèmes. ABAQUS Analysis User's Guide. Providence: Dassault Systèmes Simulia Corp., 2016
  48. Li H, Xu S. Determination of energy consumption in the fracture plane of ultra high toughness cementitious composite with direct tension test. *Engineering Fracture Mechanics*, 2011, 78(9): 1895–1905
  49. Yu J, Lu C, Chen Y, Leung C K Y. Experimental determination of crack-bridging constitutive relations of hybrid-fiber strain-hardening cementitious composites using digital image processing. *Construction and Building Materials*, 2018, 173: 359–367
  50. Genikomsou A S, Polak M A. Finite element analysis of punching shear of concrete slabs using damaged plasticity model in ABAQUS. *Engineering Structures*, 2015, 98: 38–48
  51. International Federation for Structural Concrete (*fib*). *fib* Model Code for Concrete Structures 2010. Lausanne: International Federation for Structural Concrete (*fib*), 2013
  52. Huang J Q, Dai J G. Flexural performance of precast geopolymer concrete sandwich panel enabled by FRP connector. *Composite Structures*, 2020, 248: 112563
  53. Kabir M I, Lee C K, Rana M M, Zhang Y X. Flexural and bond-slip behaviours of engineered cementitious composites encased steel composite beams. *Journal of Constructional Steel Research*, 2019, 157: 229–244
  54. Xu S, Mu F, Wang J, Li W. Experimental study on the interfacial bonding behaviors between sprayed UHTCC and concrete substrate. *Construction and Building Materials*, 2019, 195: 638–649
  55. Li Q H, Yin X, Huang B T, Luo A M, Lyu Y, Sun C J, Xu S L. Shear interfacial fracture of strain-hardening fiber-reinforced cementitious composites and concrete: A novel approach. *Engineering Fracture Mechanics*, 2021, 253: 107849
  56. Huang J Q, Dai J G. Direct shear tests of glass fiber reinforced polymer connectors for use in precast concrete sandwich panels. *Composite Structures*, 2019, 207: 136–147
  57. Khan M K I, Lee C K, Zhang Y X. Numerical modelling of engineered cementitious composites-concrete encased steel composite columns. *Journal of Constructional Steel Research*, 2020, 170: 106082
  58. Othman H, Marzouk H. Finite-element analysis of reinforced concrete plates subjected to repeated impact loads. *Journal of Structural Engineering*, 2017, 143(9): 04017120
  59. Xu L Y, Huang B T, Li V C, Dai J G. High-strength high-ductility Engineered/Strain-Hardening Cementitious Composites (ECC/SHCC) incorporating geopolymers fine aggregates. *Cement and Concrete Composites*, 2022, 125: 104296
  60. Xu S L, Xu H L, Huang B T, Li Q H, Yu K Q, Yu J T. Development of ultrahigh-strength ultrahigh-toughness cementitious composites (UHS-UHTCC) using polyethylene and steel fibers. *Composites Communications*, 2022, 29: 100992